



Exploring the electrical transport properties of $\text{La}_{0.67}\text{Ca}_{0.33}\text{MnO}_3$ at different sintering temperatures

Longfei Qi¹, Yule Li¹, Ping Yu¹, Xiaojin Wang¹, Yingjuan Li¹, Yan Gao¹, Yunrui Yang¹, Dingzhang Wu¹, Hui Zhang¹, and Qingming Chen^{1,*} 

¹ Faculty of Materials Science and Engineering, Kunming University of Science and Technology, Kunming 650093, Yunnan, China

Received: 8 January 2021

Accepted: 7 April 2021

Published online:

3 June 2021

© The Author(s), under exclusive licence to Springer Science+Business Media, LLC, part of Springer Nature 2021

ABSTRACT

The $\text{La}_{0.67}\text{Ca}_{0.33}\text{MnO}_3$ polycrystalline ceramics were prepared by the co-precipitation method with ammonium carbonate as the precipitant and the influence of the sintering temperature on the electrical transport properties of the ceramics were investigated. XRD results show that the ceramic structures obtained are all perovskite structures, which belong to the $Pnma$ space group. Scanning electron microscopy (SEM) photographs demonstrated that the average size of the grains with the sinter temperature increased from 5.78 μm at 1300 °C to 24.04 μm at 1475 °C. Meanwhile, when the sintering temperature reached 1450 °C, the TCR reached the maximal value (32.3%·K⁻¹), which was much larger than the TCR at 1350 °C. The theoretical model analysis of the data leads to the conclusion that the conductive mechanism of the low-temperature metallic region and the high-temperature insulating region is dominated by the grain boundary scattering effect and the small-polariton hopping (SPH), respectively.

1 Introduction

In recent decades, Manganese-based perovskite materials with CMR effect are another strong correlated material after high-temperature superconductors [1–5]. The general formula is $\text{RE}_x\text{AE}_{1-x}\text{MnO}_3$ (RE is the rare-earth element, La^{3+} , Nd^{3+} , etc.; AE is the alkali earth element, Ca^{2+} , Sr^{2+} , etc.) while being of extensive attention due to special physical properties, for instance, the colossal magnetoresistance effect (CMR), charge/orbital ordering, phase separation and so on [6–8]. Such properties had potential

technical applications in magnetic refrigeration, magnetic sensors, and infrared detectors [9, 10].

The Mn ion in the parent compound (RMnO_3) occupies the B position and is all + 3 valence, and the material as a whole exhibits antiferromagnetic insulating properties [11]. When doped with divalent alkaline earth ions, a mixed-valence state of Mn^{3+} and Mn^{4+} will appear in the system to hold the electric neutrality. Electrons jump between Mn^{3+} and Mn^{4+} via oxygen ions, forming a double-exchange mechanism. Since the strong coupling effect of the electron–phonon, the electrons in the process of jumping are accompanied by the movement of lattice

Address correspondence to E-mail: qmchen99@163.com

distortion, resulting in the so-called Jahn Teller effect [12–17]. In general, double-exchange interactions support metal behavior, while the Jahn–Teller effect is in favor of insulator properties [18, 19].

Many factors have a bearing on the properties of LCMO materials, such as the average radius of the A-site cation, the tolerance factor, and oxygen vacancy [20, 21]. However, in perovskite manganese oxides, oxygen vacancy exists as a defect that is easily ignored and quantified by parameter δ . Similar to the La/Ca chemical substitution, changes in oxygen content affect carrier concentration and thus transport and magnetic properties. Besides, the effect of grain boundaries in polycrystalline manganese oxides has been intensively studied, and different synthesis methods and preparation conditions can change the microstructure of ceramics such as uniformity, crystallization, and grain size, thus impacting the electrical properties of the system [22–25]. The conventional methods for the preparation of calcium-titanite manganese oxides include the conventional solid-state reaction, co-precipitation, reactive milling, spray-drying, sol–gel method, etc. [26, 27]. The co-precipitation method has the advantages of solid-phase and sol–gel methods and has the high chemical activity to accurately control the ratio of raw materials, to prepare the precursors with small particle size and uniform distribution. So it is of great significance to study the preparation of LCMO ceramics using the co-precipitation method to improve their magnetoelectric transport performance.

In the present work, LCMO was synthesized through the co-precipitation method and sintered at various temperatures. The crystallinity, microstructure, and electrical properties of these samples were investigated for all samples. The maximum *TCR* of the samples obtained by sintering at 1450 °C is close to that of the sol–gel method. Furthermore, by fitting ρ -*T*, the mechanism of the electrical properties in the metallic and insulating regions of the samples were systematically investigated.

2 Experimental

The series of LCMO ceramic samples were prepared by the co-precipitation. $\text{La}(\text{NO}_3)_3 \cdot n\text{H}_2\text{O}$, $\text{Ca}(\text{NO}_3)_2 \cdot 4\text{H}_2\text{O}$, and $\text{Mn}(\text{NO}_3)_2 \cdot 4\text{H}_2\text{O}$ were used as materials, and dissolved the required amount of these metal salts in deionized water in a stoichiometric ratio.

$(\text{NH}_4)_2\text{CO}_3$ was also dissolved in deionized water as a precipitant, and the two cups of solution were stirred continuously on a magnetic stirrer until homogeneous clarification. Poured the mixture of $\text{La}(\text{NO}_3)_2$, $\text{Ca}(\text{NO}_3)_2$ and $\text{Mn}(\text{NO}_3)_2$ into a brown dropper and the precipitant $(\text{NH}_4)_2\text{CO}_3$ into a transparent dropper, and the reaction was carried out by co-dropping the two solutions slowly and uniformly until complete, then stirred for 30 min. Afterward, the reaction solution was left to aging for 14 h in a dark place. The aging mixture was stirred and the precipitate was evenly dispersed into the solution using an ultrasonic disperser and poured into a funnel for filtration. The filter cake was dried in an oven at 70 °C for 7 h. Then the dried material was ground for the first time using an agate mortar, and the resultant powdered white solids were calcined at 500 °C for 8 h. Finally, the calcined precursor powder was ground again, pressed into circular disks with a hydro press at 18–19 MPa. Subsequently, LCMO polycrystalline samples were sintered under different temperatures of 1350 °C, 1400 °C, 1450 °C, and 1475 °C, for approximately 12 h in a muffle furnace.

X-ray diffraction analysis of LCMO ceramics (measurement range 20°–80°, scanning speed 4°/min) was performed to obtain information on the crystalline properties and structure of the samples. The microstructure and surface morphology of the samples were characterized by scanning electron microscopy. The temperature dependence of resistance (*R*-*T*) of the sample was measured using the standard four-probe method.

3 Results and discussion

3.1 Structure and surface morphology

The *XRD* spectra of the samples prepared at different sintering temperatures are shown in Fig. 1a shows the full diffraction spectrum of LCMO ceramics. The diffraction peaks of all samples were sharp and there are no additional peaks, indicating good crystallization performance, and the structure of all samples was of orthorhombic perovskite. Figure 1b is an enlarged view of the main diffraction peak (121), from which it can be seen that the main peak is shifted to a lower angle and the cell volume should have been increased. According to the Bragg formula and the spacing formula: As the main diffraction

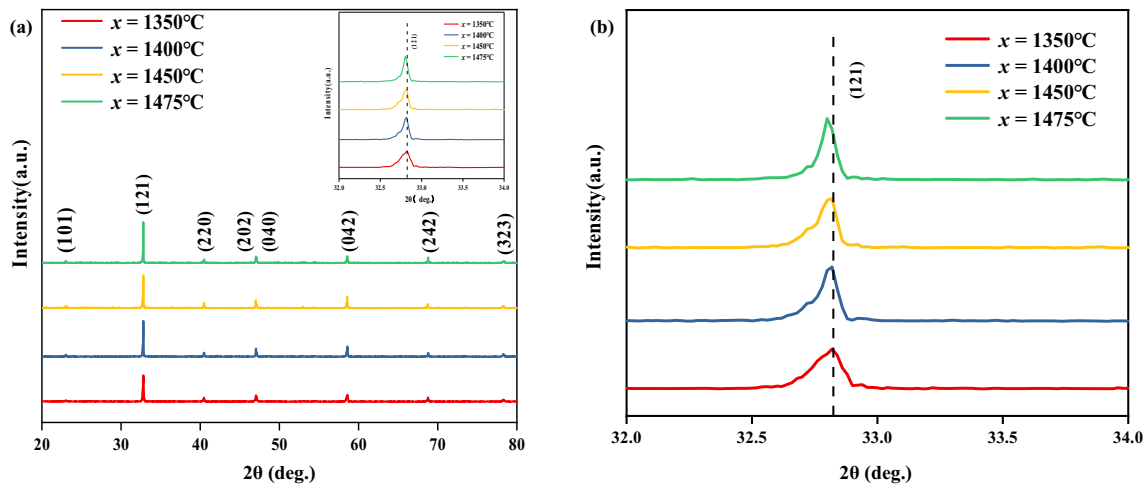


Fig. 1 **a** XRD patterns of LCMO sintered at different temperatures of 1350 °C, 1400 °C, 1450 °C, and 1475 °C. **b** enlarged view of the strongest diffraction peak

peak shifts to a lower angle, the spacing increases, indicating an increase in the cell volume V . To further confirm the altered crystal structure and increased cell volume, XRD spectra were refined for all target samples as shown in Fig. 2, and the resulting fitting parameters are listed in Table 1. From Table 1, it is observed that the cell volume shows a trend of decreasing and then increasing, which can be explained by the absorption and escape of oxygen [28]. In the same air atmosphere (with the same oxygen partial pressure), oxygen absorption plays a key role in the sample when the sintering temperature is increased from 1300 to 1400 °C. At this time, due to the increase of driving force of sintering, the lattice vibration was enhanced, and some oxygen ions diffuse into the lattice. To maintain the electrical neutrality of the system, more Mn^{3+} is converted into Mn^{4+} , resulting in a decrease in cell volume. However, when the sintering temperature rises more, the sample shows oxygen desorption, and some oxygen will escape from the lattice, showing oxygen vacancy caused by anoxic behavior. Oxygen vacancy is a positively charged hole in the lattice and it has larger than negatively charged oxygen ions [29]. Therefore, desorption of oxygen will increase the unit cell volume. In Fig. 1d–h, it can be seen that the diffraction peaks of the experimental samples are in good agreement with the standard spectra, further confirming the pure-phase calcium-titanite structure of the samples.

The surface morphology of the LCMO at different temperatures (1350 °C (a), 1400 °C (b), 1450 °C

(c) and 1475 °C (d)) polycrystalline studied by SEM are given in Fig. 3a–d.

Figure 4a–e shows the grain size of LCMO at different temperatures of 1350 °C (a), 1400 °C (b), 1450 °C (c), and 1475 °C (d). Due to the large grain size of LSMO, to better count the grain size of the material using Nona measurer 1.2 software, then analyze the grain size trends for this series of samples, the SEM image of LSMO at 2000-times magnification was used. It can be seen from the figure that with the increase of sintering temperature, the material becomes denser and the grain size increases. This is mainly because the increase in sintering temperature provides sufficient energy for cell formation and growth, which in turn leads to a decrease in porosity and an increase in crystallinity and density. Meanwhile, with the increase of sintering temperature, the amount of oxygen required increases, resulting in the oxygen deficiency of the samples, which will lead to the increase of grain size [30]. The increase in grain size also leads to a decrease in grain boundaries, which affects the scattering of electrons at the grain boundaries. The grain boundary is highly connected and the reduction in quantity ensures that the material has good electrical properties.

3.2 Temperature dependence of electrical properties (ρ - T)

The resistivity-temperature curves for these samples under different sintering temperatures are shown in Fig. 5. As can be seen in the figure, all samples show

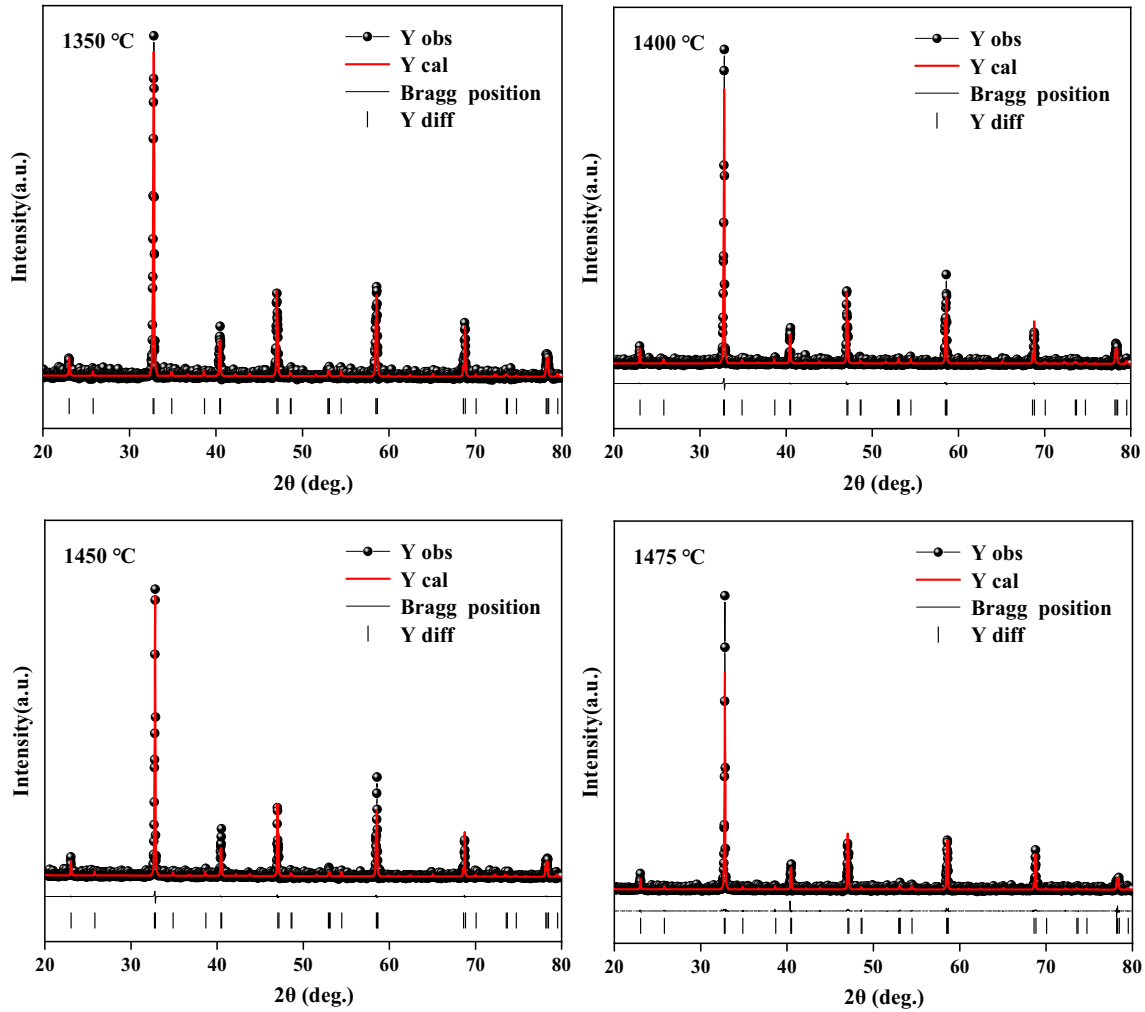


Fig. 2 Rietveld refinement plots of LCMO at different temperatures

Table 1 Structure of LCMO samples and refinement parameters of their XRD

x (temperature)	1350 °C	1400 °C	1450 °C	1475 °C
Space group	Pnma	Pnma	Pnma	Pnma
Lattice constant (Å)				
a	5.45270	5.45170	5.45830	5.45430
b	7.70580	7.70410	7.71250	7.70490
c	5.48330	5.48470	5.48460	5.48270
Cell volume (Å ³)				
V	231.1935	231.6160	231.6958	231.5674
Bond angles (°)				
Mn–O–Mn	160.6193	160.6312	160.6323	160.6365
Fit index/%				
R _e	17.3475	18.0269	17.9225	17.9763
R _b	5.1152	3.7299	4.5378	3.8116
R _p	12.4464	13.2167	13.2697	12.6628
χ	0.85917	0.88818	0.90503	0.8341

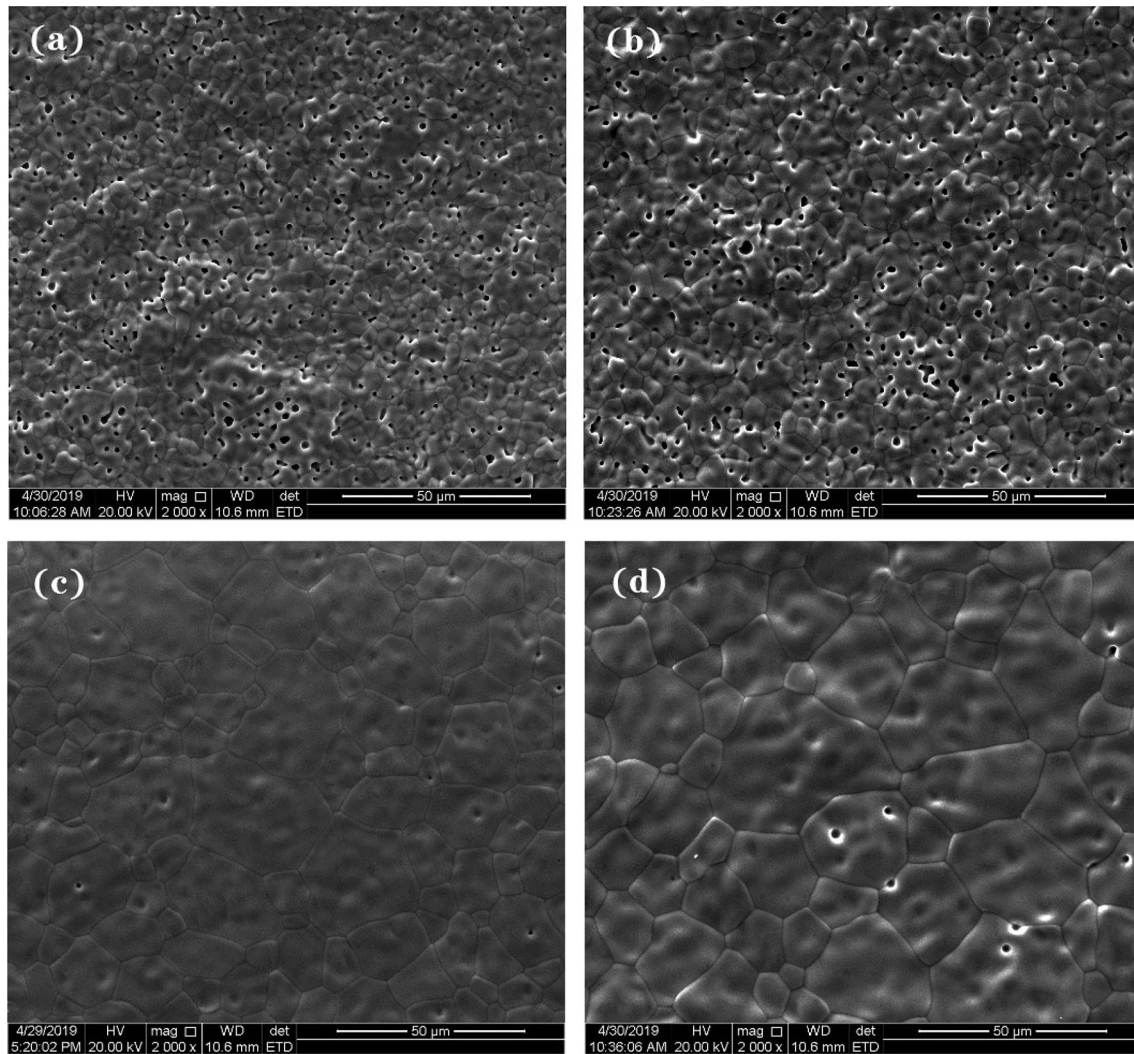


Fig. 3 FESSEM images(magnification at $\times 2.00$ K) of LCMO composites at different temperatures of 1350 °C (a), 1400 °C (b), 1450 °C (c) and 1475 °C (d)

similar resistivity trends. As the testing temperature increases, the target is gradually transformed from a ferromagnetic metallic phase at low temperatures to a paramagnetic insulating phase at high temperatures. On the other hand, T_p also showed almost the same change trend as the cell volume. This may be due to the gradual formation of more oxygen vacancies in the sample with the increase of sintering temperature, resulting in the reduction of Mn^{4+} and the generation of point defects in the structure. Therefore, by changing the bond length and bond angle between manganese ions, the double-exchange effect is weakened, shifting T_p to the low-temperature side. As is well-known, the grain size and the connections between the grains play a important role in electron conduction [31]. With the gradual increase of the

sintering temperature, the resistivity of the corresponding sample gradually decreases, from 0.03338 Ω at 1350 °C to 0.01806 Ω at 1475 °C. The reason is, raising the sintering temperature promotes grain growth and amalgamation, reduces porosity, and improves intergrain contact. Meanwhile, based on the double-exchange model, Mn^{3+} and Mn^{4+} in LCMO transfer charge through oxygen ions, and the local change of oxygen vacancy concentration will lead to the change of resistivity [32]. Therefore, with the increase of sintering temperature T_a , some crystal cells in LCMO may form oxygen vacancies due to the lack of oxygen, which increases oxygen ion mobility. Thus, the sample exhibits an increase in electrical conductivity.

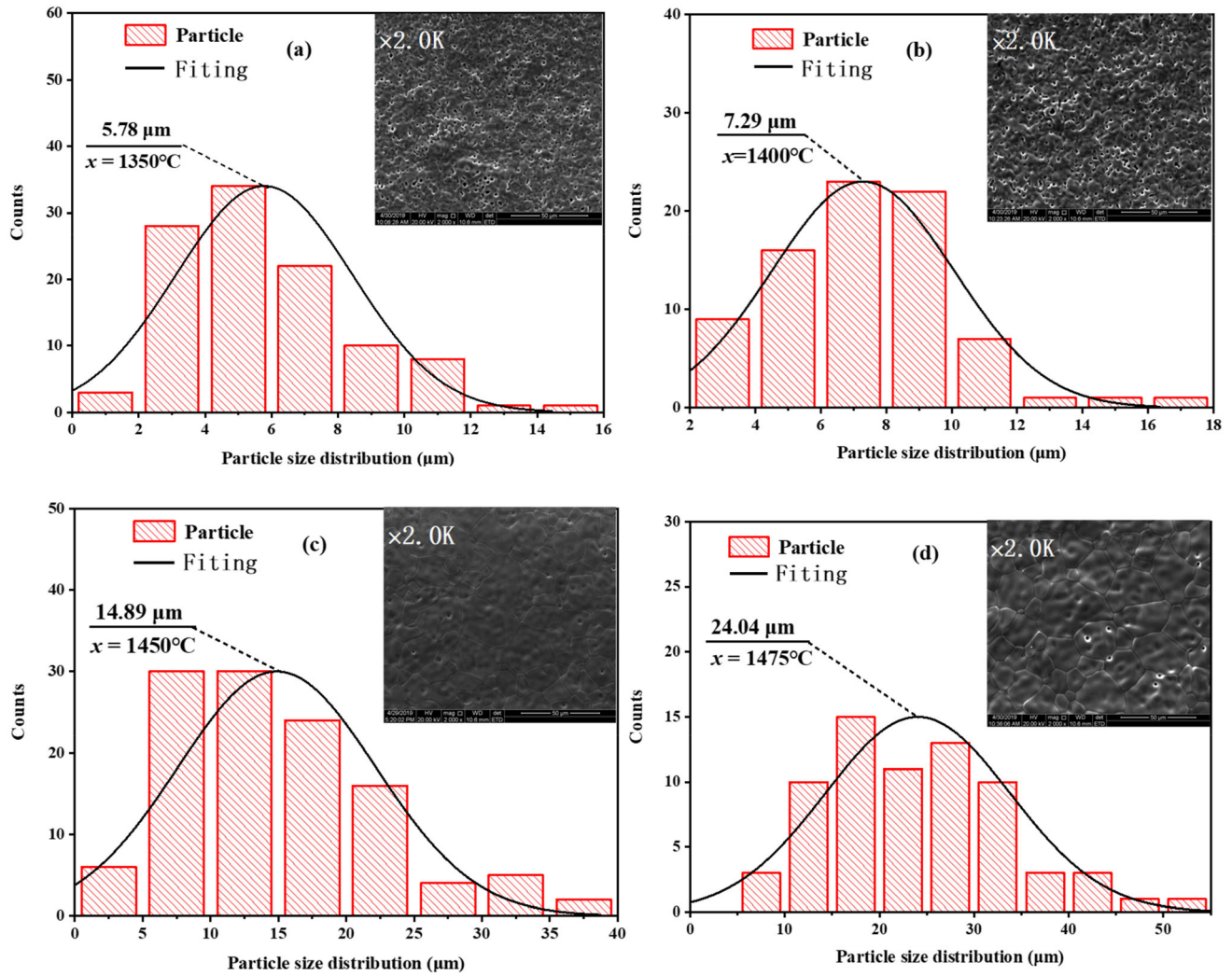


Fig. 4 The grain size of LCMO samples prepared at different temperatures of 1350 °C (a), 1400 °C (b), 1450 °C (c), and 1475 °C (d)

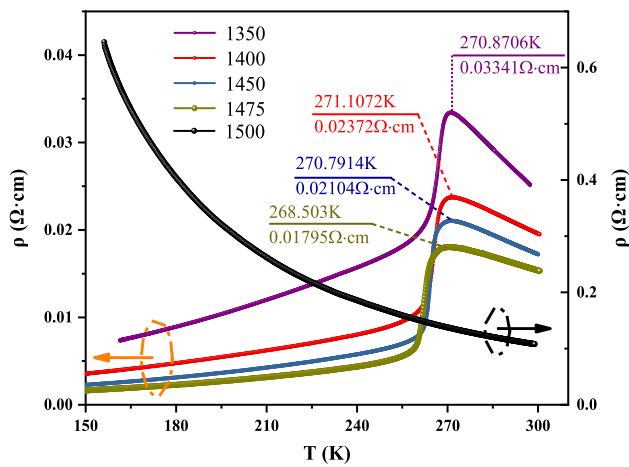


Fig. 5 Resistivity versus temperature plots of LCMO samples

3.3 Temperature coefficient of resistivity (TCR)

Based on the above discussion, it can be seen that the steepness of the R - T curve transition varies for these samples with the temperature reaching T_p . To explain this phenomenon, the resistive temperature coefficient TCR has been investigated, which can be defined by Eq. (1):

$$TCR = \frac{1}{\rho} \cdot \frac{d\rho}{dT} \times 100\% \quad (1)$$

where ρ is the resistivity and T is the temperature.

Figure 6 shows the TCR curve of LCMO samples. TCR_{max} tended to increase and then decrease at different sintering temperatures. The TCR reached the maximum of $32.3\% \cdot K^{-1}$ for the sintering temperature

of 1450 °C. Furthermore, it is noteworthy that the transition broadening temperature (ΔT) becomes progressively narrower along with increasing sintering temperature. (ΔT) depicts the temperature range during the metal-insulation transition. Resistivity changes concerning grain boundaries, yet (ΔT) is determined by the degree of synchronization within the grain boundaries or between different grains. This can be explained by the homogeneity within the polycrystal, where the more grain boundaries there are, the less homogeneous the sample will be. In the increase of sintering temperature from 1350 °C to 1450 °C, the ratio of $\text{Mn}^{4+}/\text{Mn}^{3+}$ in the samples increased, resulting in an enhanced double-exchange interaction. Meanwhile, the grain size increases and the grain boundaries decrease, thus improving the uniformity of the sample and contributing to the enhancement of TCR . However, when the temperature is increased to 1475 °C, the increase of oxygen vacancy, the vacancy states formed by Mn and O in the cell where the vacancy is located destroy the spin polarization, which affects the metallicity of LCMO. In the meantime, the crystallinity of the sintered sample may decrease, which may manifest itself as a decrease in TCR . Which was noted (seen in Fig. 5) that at the sintering temperature of 1500 °C, the samples exhibited no metallic-insulation transition and showed insulating properties. It is confirmed that the sintering temperature of 1500 °C exceeds the melting point of $\text{La}_{0.67}\text{Ca}_{0.33}\text{MnO}_3$ ceramics, not suitable as a conventional sintering temperature. By combining the electrical properties of the sintering

temperature of 1450 °C and 1475 °C, 1450 °C was selected as the conventional sintering temperature for $\text{La}_{0.67}\text{Ca}_{0.33}\text{MnO}_3$.

3.4 Conduction mechanism

To better understand the electrical transport mechanism of LCMO, the ρ - T curve of the sample is divided into the metallic phase region ($T < T_p$) and the insulating phase region ($T > T_p$). The experimental data in different temperature regions have been combined with the corresponding formula model for the fit analysis.

3.4.1 Low-temperature range

The samples have presented in the metallic phase at low temperatures. To study the influence of the scattering mechanism on the resistivity of the sample, the resistivity data were fitted in the low-temperature phase by Eq. (2) [33, 34]:

$$\rho_{\text{FM}}(T) = \rho_0 + \rho_2 T^2 + \rho_{4.5} T^{4.5} \quad (2)$$

where ρ_0 is the residual resistivity, mainly due to grain boundary scattering, $\rho_2 T^2$ is the scattering effect between electrons and electrons. $\rho_{4.5} T^{4.5}$ represents the complex scattering interaction to the combination of electron, phonon and magneton. The fitting graphs at the region of $T < T_p$ are shown in Fig. 7a and the relevant parameters obtained are listed in Table 2. As seen in Table 2, the residual resistivity ρ_0 and $\rho_2 T^2$ gradually decreases as the higher the sintering temperature. This is mainly due to the increased grain size of the sample, which reduces the scattering process by decreasing the quantity of grain boundaries, corresponding to the SEM results. The magnitude (seen in Table 2) could be observed that $\rho_0 > \rho_2 > \rho_{4.5}$. Thus, it can be demonstrated that an increase in grain size can reduce the grain boundary region, thus decreasing the net grain boundary scattering term as well as the electron-magneton scattering term. This explored that the residual resistivity ρ_0 due to grain boundary scattering in this low-temperature range ($T < T_p$) is the dominant factor in the electrical transport performance of the sample.

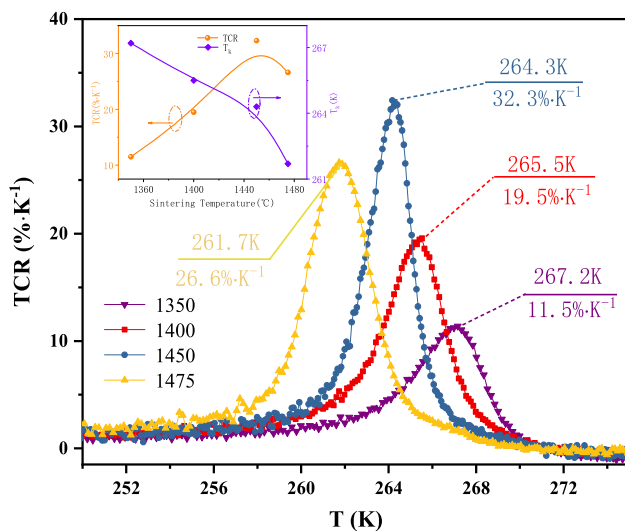


Fig. 6 TCR versus temperature plots of LCMO samples

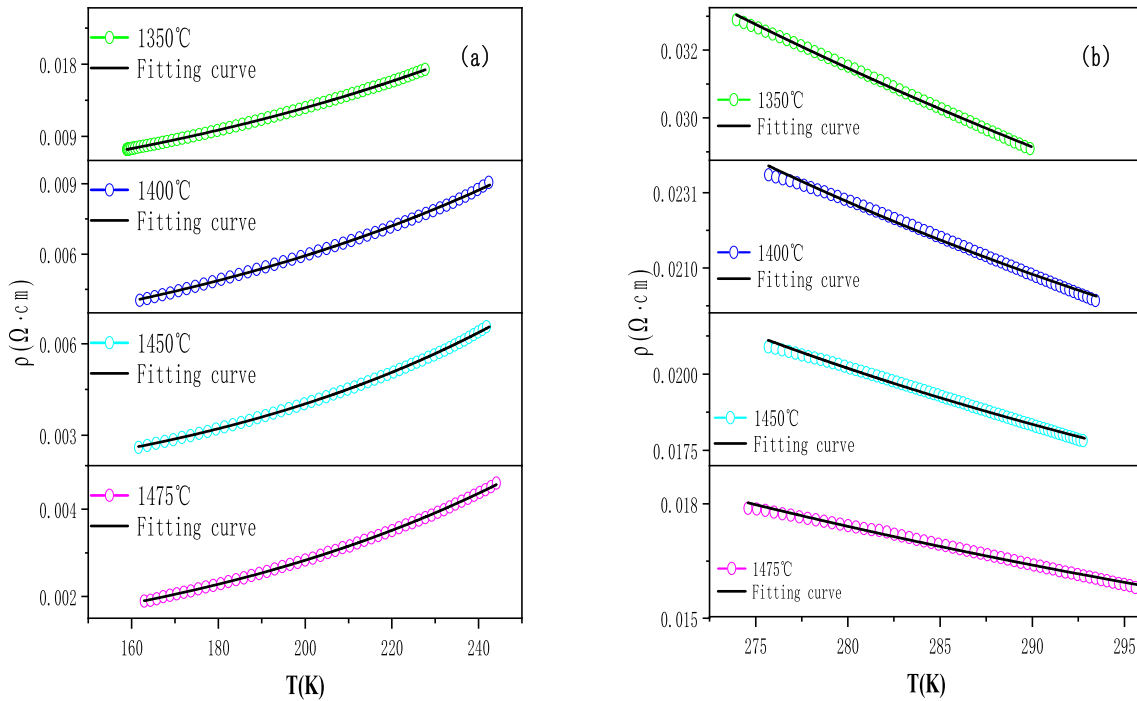


Fig. 7 Fitting electrical resistivity curve in ranges of $T < T_p$ (a), $T > T_p$ (b)

Table 2 Low-temperature fitting parameters obtained from fitting experimental data with Eq. (2)

Temperature (°C)	$\rho_0/(\Omega\cdot\text{cm}) \cdot 10^{-3}$	$\rho_2/(\Omega\cdot\text{cm}\cdot\text{K}^{-1}) \cdot 10^{-10}$	$\rho_{4.5}/(\Omega\cdot\text{cm}\cdot\text{K}^{-1})\cdot 10^{-15}$	R^2
(1) ($T < T_p$)				
1350	1.3	2217.57	32.1491	0.9997
1400	1.42	906.82	27.8364	0.9995
1450	0.95	506.743	37.5235	0.9997
1475	0.59	394.138	29.2903	0.9999

3.4.2 High-temperature range

To investigate the mechanism of ρ - T in the paramagnetic high-temperature region ($T > T_p$), the ρ - T were fitted through the small-polaron hopping model as Eq. (3):

$$\rho_{PM}(T) = \rho_{0s} T \exp(E_a/k_B T) \tag{3}$$

where ρ_{0s} is the resistivity coefficient, E_a is the small-polaron activation energy and k_B is Boltzmann constant. The model fitting result is shown in Fig. 7b. The parameters are presented in Table 3. As seen, with the sintering temperature increasing, the overall activation energy E_a tends to decrease. Widely known, the interconnectivity between the grains increases with the grain size increasing, which will increase the likelihood that conductive electrons jump to neighboring positions. Also, the sintering drive at high sintering temperatures makes the

Table 3 SPH model fitting parameters obtained from fitting experimental data through Eq. (3)

Temperature (°C)	E_a/meV	R^2
(2) ($T > T_p$)		
1350	9.72044	0.9979
1400	7.57056	0.9993
1450	7.73463	0.9946
1475	6.66538	0.9937

conduction electrons more prone to transition. This increases the number of carriers excited from the valence band to the conduction band, leading to a decrease in the activation energy E_a , and thus causing a change in the electrical transport properties of the sample.

4 Conclusion

In this paper, the effects of sintering temperature on the electron transport properties of $\text{La}_{0.67}\text{Ca}_{0.33}\text{MnO}_3$ ceramics prepared by co-precipitation were studied. XRD analysis demonstrated that all polycrystalline samples belong to the orthorhombic calcite structure with a space group, with good crystallization properties. SEM images showed that the samples with different sintering temperatures have a higher density and larger grain sizes at higher temperatures, which is the main reason for the decreased resistivity. The highest TCR ($\text{TCR}_{\text{max}} = 32.3\% \cdot \text{K}^{-1}$) is obtained at a sintering temperature of 1450 °C. The analysis shows that the combined effect of the oxygen vacancy and grain size might be responsible for the observed electrical behavior. The conduction mechanism in the low-temperature region ($T < T_p$) can use the grain boundary scattering effect of the sample to explain, and the ρ - t curve in the high-temperature region can be fitted by the adiabatic small dipole model.

Acknowledgements

This work was supported by the National Natural Science Foundation of China (No.11564021).

Declarations

Conflict of interest No conflict of interest exists in the submission of this manuscript, and manuscript is approved by all authors for publication.

References

1. E. Rozenberg, M. Auslender, A.I. Shames, Y.M. Mukovskii, E. Sominski, A. Gedanken, Specific effects of nanometer scale size on magnetic ordering in $\text{La}_{1-x}\text{Ca}_x\text{MnO}_3$ ($x=0.1, 0.3$ and 0.6) manganites. *J. Non Cryst. Solids* **354**, 5282 (2008). <https://doi.org/10.1016/j.jnoncrsol.2008.05.087>
2. Q. Zhou, M. Dai, R. Wang et al., Enhancement of magnetoresistance in Mn substituted $\text{La}_{2/3}\text{Sr}_{1/3}\text{Mn}_{1-x}\text{Zr}_x\text{O}_3$ granular system. *Phys. B* **371**, 120 (2006). <https://doi.org/10.1016/j.physb.2005.09.030>
3. S.P. Altintas, A. Amira, C. Terzioglu, Structural characterization and magneto electrical behavior of Sm doped $\text{La}_{0.7}\text{Ca}_{0.3}\text{MnO}_3$ manganites. *J. Supercond. Nov. Magn.* **26**, 1461 (2012). <https://doi.org/10.1007/s10948-012-2065-4>
4. J. Ma, Y. Cai, W. Wang et al., Enhancement of temperature coefficient of resistivity in $\text{La}_{0.67}\text{Ca}_{0.33}\text{MnO}_3$ polycrystalline ceramics. *Ceram. Int.* **40**, 4963 (2014). <https://doi.org/10.1016/j.ceramint.2013.10.105>
5. S. Vadnala, P. Pal, S. Asthana, Investigation of near room temperature magnetocaloric, magnetoresistance and bolometric properties of $\text{Nd}_{0.5}\text{La}_{0.2}\text{Sr}_{0.3}\text{MnO}_3$: Ag₂O manganites. *J. Mater. Sci. Mater. Electron.* **27**, 6156 (2016). <https://doi.org/10.1007/s10854-016-4543-0>
6. N. Raju, D.R. Sree, S.S.K. Reddy et al., Nanosize effects on the magnetic field induced transitions in $\text{La}_{0.67-x}\text{Eu}_x\text{Ca}_{0.33}\text{MnO}_3$ perovskite manganite. *J. Magn. Magn. Mater.* **368**, 308 (2014). <https://doi.org/10.1016/j.jmmm.2014.05.029>
7. S. Zhao, X. Yue, X. Liu, Tuning room temperature T_p and MR of $\text{La}_{1-y}(\text{Ca}_y\text{Sr}_x)\text{MnO}_3$ polycrystalline ceramics by Sr doping. *Ceram Int.* **43**, 4594 (2017). <https://doi.org/10.1016/j.ceramint.2016.12.121>
8. K. Navin, R. Kurchania, The effect of particle size on structural, magnetic and transport properties of $\text{La}_{0.7}\text{Sr}_{0.3}\text{MnO}_3$ nanoparticles. *Ceram Int.* **44**, 4973 (2018). <https://doi.org/10.1016/j.ceramint.2017.12.091>
9. D.J. Singh, W.E. Pickett, Lattice effects in ferromagnetic manganite perovskites. *J. Appl. Phys.* **83**, 7354 (1998). <https://doi.org/10.1063/1.367678>
10. P. Zhang, T.L. Phan, S.C. Yu, Magnetocaloric Effect in $\text{La}_{0.7}\text{Cd}_{0.3}\text{MnO}_3$, $\text{La}_{0.7}\text{Ba}_{0.3}\text{MnO}_3$, and $\text{Nd}_{0.7}\text{Sr}_{0.3}\text{MnO}_3$. *J. Supercond. Nov. Magn.* **25**, 2727 (2011). <https://doi.org/10.1007/s10948-011-1252-z>
11. J.C. Debnath, A.M. Strydom, Transport-entropy correlations in $\text{La}_{0.7}\text{Ca}_{0.3}\text{MnO}_3$ manganite. *Phys. B* **432**, 96 (2014). <https://doi.org/10.1016/j.physb.2013.09.045>
12. Y. Zhou, X. Zhu, S. Li, Structure, magnetic, electrical transport and magnetoresistance properties of $\text{La}_{0.67}\text{Sr}_{0.33}\text{Mn}_{1-x}\text{Fe}_x\text{O}_3$ ($x=0-0.15$) doped manganite coatings. *Ceram Int.* **43**, 3679 (2017). <https://doi.org/10.1016/j.ceramint.2016.11.210>
13. T.L. Phan, P.S. Tola, N.T. Dang, J.S. Rhyee, W.H. Shon, T.A. Ho, Tricritical behavior and Griffith phase in $\text{La}_{1-x}\text{Ca}_x\text{MnO}_3$ under high applied fields. *J. Magn. Magn. Mater.* **441**, 290 (2017). <https://doi.org/10.1016/j.jmmm.2017.05.088>
14. P.S. Solanki, R.R. Doshi, A. Ravalia et al., Transport studies on $\text{La}_{0.8-x}\text{Pr}_{0.2}\text{Sr}_x\text{MnO}_3$ manganite films. *Phys. B* **465**, 71 (2015). <https://doi.org/10.1016/j.physb.2015.02.019>
15. V. Ferrari, J.M. Pruneda, E. Artacho, Density functionals and half-metallicity in $\text{La}_{2/3}\text{Sr}_{1/3}\text{MnO}_3$. *Phys. Status Solidi A* **203**, 1437 (2006). <https://doi.org/10.1002/pssa.200566183>
16. G. Jung, V. Markovich, D. Mogilyanski, C. van der Beek, Y.M. Mukovskii, Ferromagnetic and twin domains in LCMO manganites. *J. Magn. Magn. Mater.* **290–291**, 902 (2005). <https://doi.org/10.1016/j.jmmm.2004.11.285>

17. F.L. Tang, X. Zhang, Y. Shao, Sr ion distribution and local structure in $\text{La}_{1-x}\text{Sr}_x\text{MnO}_3$. *J. Phys. Condens. Matter* **18**, 5579 (2006). <https://doi.org/10.1088/0953-8984/18/23/026>
18. J. Ma, M. Theingi, H. Zhang, X. Ding, Q. Chen, Structural and electrical characterization of $\text{La}_{0.72}\text{Ca}_{0.28}\text{MnO}_3$ ceramic and thin films. *Appl. Surf. Sci.* **264**, 225 (2013). <https://doi.org/10.1016/j.apsusc.2012.09.177>
19. H.Y. Hwang, S.W. Cheong, P.G. Radaelli, M. Marezio, B. Batlogg, Lattice effects on the magnetoresistance in doped LaMnO_3 . *Phys. Rev. Lett.* **75**, 914 (1995). <https://doi.org/10.1103/PhysRevLett.75.914>
20. T. Geng, N. Zhang, Electronic structure of the perovskite oxides $\text{La}_{1-x}\text{Sr}_x\text{MnO}_3$. *Mod. Phys. Lett.* **351**, 314 (2006). <https://doi.org/10.1016/j.physleta.2005.10.095>
21. J. Sakai, N. Ito, S. Imai, Oxygen content of $\text{La}_{1-x}\text{Sr}_x\text{MnO}_{3-y}$ thin films and its relation to electric-magnetic properties. *J. Appl. Phys.* (2006). <https://doi.org/10.1063/1.2176323>
22. V.P.S. Awana, R. Tripathi, S. Balamurugan, H. Kishan, E. Takayama-Muromachi, Magneto-transport of high TCR (temperature coefficient of resistance) $\text{La}_2/3\text{Ca}_1/3\text{MnO}_3$: Ag polycrystalline composites. *Solid State Commun.* **140**, 410 (2006). <https://doi.org/10.1016/j.ssc.2006.09.021>
23. R. Søndena, P. Ravindran, S. Stølen, T. Grande, M. Hanfland, Electronic structure and magnetic properties of cubic and hexagonal SrMnO_3 . *Phys. Rev. B* (2006). <https://doi.org/10.1103/PhysRevB.74.144102>
24. P. Nisha, S.S. Pillai, M.R. Varma, K.G. Suresh, Influence of cobalt on the structural, magnetic and magnetocaloric properties of $\text{La}_{0.67}\text{Ca}_{0.33}\text{MnO}_3$. *J. Magn. Magn. Mater* **327**, 189 (2013). <https://doi.org/10.1016/j.jmmm.2012.09.029>
25. G.F. Wang, L.R. Li, Z.R. Zhao, X.Q. Yu, X.F. Zhang, Structural and magnetocaloric effect of $\text{Ln}_{0.67}\text{Sr}_{0.33}\text{MnO}_3$ ($\text{Ln}=\text{La, Pr and Nd}$) nanoparticles. *Ceram. Int* **40**, 16449 (2014). <https://doi.org/10.1016/j.ceramint.2014.07.154>
26. F. Jin, H. Zhang, Q. Chen, Improved Curie temperature and temperature coefficient of resistance (TCR) in $\text{La}_{0.7}\text{Ca}_{0.3-x}\text{Sr}_x\text{MnO}_3$:Ag0.2 composites. *J. Alloys Compd* **747**, 1027 (2018). <https://doi.org/10.1016/j.jallcom.2018.03.117>
27. L. Li, H. Zhang, X. Liu et al., Structure and electromagnetic properties of $\text{La}_{0.7}\text{Ca}_{0.3-x}\text{K}_x\text{MnO}_3$ polycrystalline ceramics. *Ceram. Int* **45**, 10558 (2019). <https://doi.org/10.1016/j.ceramint.2019.02.120>
28. X.F. Song, G.J. Lian, G.C. Xiong, Small polaronic transport in oxygen-deficient $\text{La}_{0.7}\text{Ca}_{0.3}\text{MnO}_{3-\delta}$ thin films. *Phys. Rev. B* (2005). <https://doi.org/10.1103/PhysRevB.71.214427>
29. J. Zhao, C. Liu, J. Li et al., Oxygen vacancy induced electronic structure variation in the $\text{La}_{0.2}\text{Sr}_{0.8}\text{MnO}_3$ thin film. *AIP Adv* (2019). <https://doi.org/10.1063/1.5088738>
30. D.R.S.B.K. Roul, S. Mohanty, A.K. Pradhan, Effect of high temperature sintering schedule for enhanced CMR properties of $\text{La}_{0.67}\text{Ca}_{0.33}\text{MnO}_3$ close to room temperature. *Mater. Chem. Phys* **67**, 267 (2001)
31. J.S. Park, C.O. Kim, Y.P. Lee et al., Influence of grain size on the electronic and the magnetic properties of $\text{La}_{0.7}\text{Ca}_{0.3}\text{MnO}_{3-\delta}$. *J. Appl. Phys* **96**, 2033 (2004). <https://doi.org/10.1063/1.1774264>
32. Y.B. Nian, J. Strozier, N.J. Wu, X. Chen, A. Ignatiev, Evidence for an oxygen diffusion model for the electric pulse induced resistance change effect in transition-metal oxides. *Phys Rev Lett* **98**, 146403 (2007). <https://doi.org/10.1103/PhysRevLett.98.146403>
33. G.K. Venkataiah, D.C. Vithal, M. Rao, S.S. Bhat, S.V. Prasad, V. Subramanyam, S.V. Reddy, Effect of sintering temperature on electrical transport properties of $\text{La}_{0.67}\text{Ca}_{0.33}\text{MnO}_3$. *Phys. B* **357**, 370 (2005). <https://doi.org/10.1016/j.physb.2004.12.001>
34. S.B. Li, C.B. Wang, H.X. Liu et al., Effect of sintering temperature on structural, magnetic and electrical transport properties of $\text{La}_{0.67}\text{Ca}_{0.33}\text{MnO}_3$ ceramics prepared by Plasma Activated Sintering. *Mater. Res. Bull* **99**, 73 (2018). <https://doi.org/10.1016/j.materresbull.2017.10.049>

Publisher's Note Springer Nature remains neutral with regard to jurisdictional claims in published maps and institutional affiliations.